Hover/Low Speed Dynamics Model Identification of a Coaxial Tricopter in Hover using Joint Input-Output Technique

Sung Hyeok Cho
Undergraduate Student
Cal Poly Pomona
Pomona, CA, USA

Vanessa D. Gonzalez
Undergraduate Student
Cal Poly Pomona
Pomona, CA, USA

Subodh Bhandari
Professor
Cal Poly Pomona
Pomona, CA, USA

Mark B. Tischler
Senior Scientist
Aviation Development Directorate
U.S. Army CCDC, AvMC
Moffett Field, CA, USA

Kenny K. Cheung
Technical Area Lead, Aeroflightdynamics
Universities Space Research Association
Moffett Field, CA, USA

ABSTRACT

This paper presents the identification and verification of the hover/low speed dynamics model of a 3DR Y6 tricopter, a coaxial tricopter, using Joint Input-Output (JIO) frequency-domain identification technique. Dynamics models for both the Y6A and Y6B configurations, which have differing rotational directions for the rear propellers, were identified. Flight data showed highly coupled dynamics and required use of JIO technique to eliminate the effect of the highly cross-correlated inputs. The identified models were verified using doublet flight data. Identification results showed that both the Y6A and Y6B configurations had highly coupled hover dynamics, different from conventional multirotor and coaxial quadrotor dynamics.

NOTATION

$a_{x, y, z}$ - Body Axis Acceleration (ft/s^2)

Hz – Hertz

Kv - Motor Rating (RPM/Volts)

L - Rolling Moment (lb ft^2/s^2)

M - Pitching Moment (lb ft^2/s^2)

mAh - milliAmp Hours

N - Yawing Moment (lb ft^2/s^2)

p - Roll Rate (rad/s)

q - Pitch Rate (rad/s)

r - Yaw Rate (rad/s)

u - Longitudinal Body Velocity (ft/s)

v - Lateral Body Velocity (ft/s)

X - Longitudinal Body Force (lb ft/s^2)

Y - Lateral Body Force (lb ft/s^2)

Z - Vertical Body Force (lb ft/s^2)

Θ - Pitch Angle (rad)

Φ - Roll Angle (rad)

ψ - Yaw Angle (rad)

δ_{col} - Collective, Throttle Mixer Input (%)

δ_{lat} – Lateral, Roll Mixer Input (%)

δ_{lon} – Longitudinal, Pitch Mixer Input (%)

δ_{ped} – Pedal, Yaw Mixer Input (%)

δ_{thr} – Throttle, Pilot Throttle Input (%)

INTRODUCTION

Research into the stability and control characteristics of coaxial multirotor unmanned aerial vehicles (UAVs) is still lacking compared to other multirotor configurations. To better understand the flight dynamics of multirotors in coaxial configurations as well as design optimal control systems, unconventional configurations and their dynamics must be accounted for. The coaxial tricopter configuration is unique in that it has multiple sub-configurations depending on the arrangement of rotors.

This paper presents the flight testing, data collection, data processing, and identification and verification of flight dynamics models of the 3DR Y6 tricopter in hover/low speed using the CIFER® (Comprehensive Identification from Frequency Responses) (Ref. 1) software package in conjunction with the Joint Input-Output (JIO) method (Ref. 2). A comparison of the results with that of a similar coaxial multicopter is also presented.

FLIGHT VEHICLE AND FLIGHT TESTING

3DR Y6 Coaxial Tricopter

The 3DR Y6, shown in Figure 1, is a coaxial tricopter which utilizes 6 motors in a three motor boom configuration. The vehicle is equipped with a Pixhawk 2.1 flight controller operating a modified ArduCopter firmware capable of performing automated maneuvers, as well as logging flight data at 100 Hz. Table 1 shows the vehicle specifications.

Figure 1. 3DR Y6.

Table 1. 3DR Y6 Aircraft Characteristics.

Characteristic	Value
Dimensions	22" x 18.5" x 9"
Empty Weight	3.41 lb
Takeoff Weight	4.80 lb
Propellers	11"
Flight Controller	Pixhawk 2.1
Firmware	ArduCopter 3.5.1
Motor	880 Kv x 6
Configuration	Y6A, Y6B

The Y6 configuration has two sub-configurations, Y6A and Y6B as shown in Figure 2 (Ref. 3). The only difference between the two sub-configurations is the rotational direction of the propellers of the rear boom. The two sub-configurations are illustrated in Figure 2.
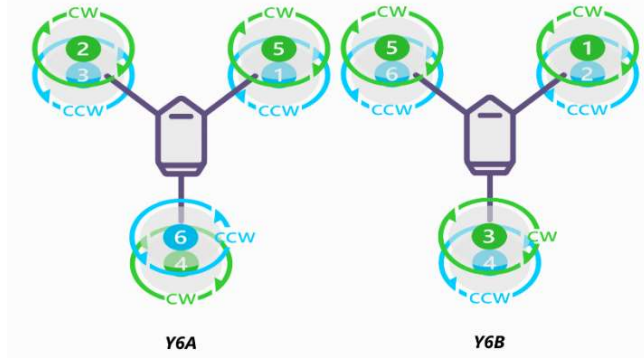

Figure 2. Illustration of Y6A and Y6B Configurations.

Flight Testing and Data Collection

The tricopter was flown in an automated frequency sweep maneuver that gradually increased the frequency from 0.5 rad/s to 60 rad/s on each axis. The tricopter was flown in ArduCopter's stock "Stabilize" (Attitude Command/Attitude Hold) flight mode, with default gains. In addition, doublet flight data was also collected using an automated maneuver for the verification of the identified models. The sensors were placed close to the center of gravity (c.g.) location, eliminating the need for c.g. offset corrections.

During each flight, the vehicle attitude, angular rates, body axis acceleration, velocity estimation, as well as pilot input and internal mixer output was recorded at 100 Hz. Flight data was then processed using MATLAB for unit conversion and resampling, as well as for reconstruction of body translational acceleration. The equations used to reconstruct body translational acceleration are shown below, where 0 subscript denotes initial values (Ref. 1).

$$\dot{u} = a_{x_{cg}} - W_0 q + V_0 r - (g \cos \Theta_0)\theta \qquad (1)$$

$$\dot{v} = a_{y_{cg}} - U_0 q + W_0 p + (g \cos \Theta_0)\Phi \qquad (2)$$

$$\dot{w} = a_{z_{cg}} - V_0 p + U_0 q - (g \sin \Theta_0)\theta \qquad (3)$$

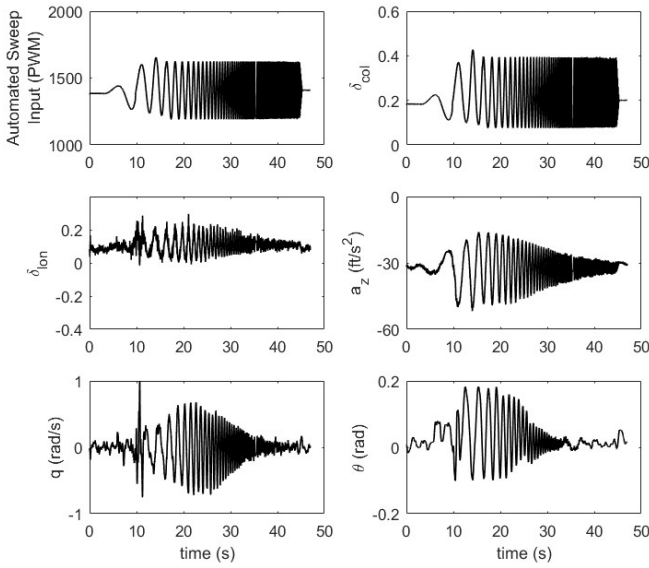Figure 3 shows frequency sweep data for a vertical sweep.

Figure 3. Frequency Sweep Data for Vertical Sweep.

As seen in Figure 3, vehicle's mixer output (input to the bare airframe) is highly coupled. In response to collective input to the vehicle, there is significant pitch rate and associated longitudinal feedback (Ref. 2). As mentioned before, the vehicle was flown in Stabilized mode as the bare airframe dynamics of multicopters is highly unstable as discussed in Ref. 4 and Ref. 5.

SYSTEM IDENTIFICATION

For the identification of the bare airframe dynamics, ArduCopter's internal mixer output was used as the actuator input for the bare airframe of the vehicle. The resulting system includes the mixer dynamics, motor dynamics, and sensor dynamics. This will be referred to as bare-airframe model throughout this paper. The bare-airframe model structure is illustrated in Figure 4 (Ref. 4).
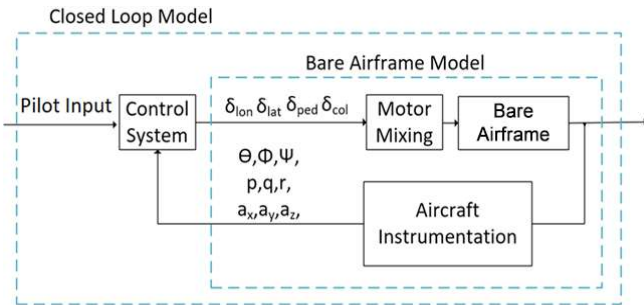

Figure 4. Structure of Bare Airframe Model.

Nonparametric Identification

When performing nonparametric frequency-domain identification for systems with highly correlated inputs, (multiple-input single-output system), the direct multi-input method cannot be used as cross-control-spectra matrix becomes singular and cannot be inverted. Also, as the dynamics are coupled, single-input single-output methods

would provide incorrect results. In this situation, Joint Input-Output (JIO) method can produce uncorrelated frequency responses, as discussed in Ref. 2.

JIO method involves the addition of uncorrelated reference inputs to the identification process, which can be external inputs from actuators, or pilot input. The process of obtaining frequency response utilizing Joint-Input Output method is,

$$\left[\frac{y}{\delta_A}(j\omega) \right] = \left[\frac{y}{r}(j\omega) \right] \left[\frac{\delta_A}{r}(j\omega) \right]^{-1} \qquad (4)$$

where δ_A stands for actuator input, and r stands for reference input. Additional details of the JIO method can be found in Ref. 2. For the purposes of the identification of Y6 flight dynamics models, automated frequency sweep inputs were used as reference inputs. The CIFER® software package was used to obtain frequency responses of reference input-output pair (Ref. 1), and JIO method was applied as a post-processing step. A sample reference input-output frequency response (y/r) is shown in Figure 5, and a sample input-output frequency response (y/δ_A) obtained through JIO method is shown in Figure 6.
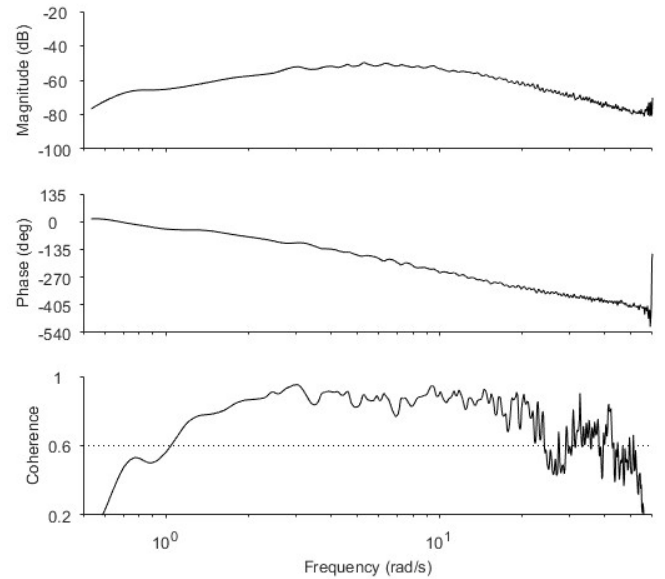

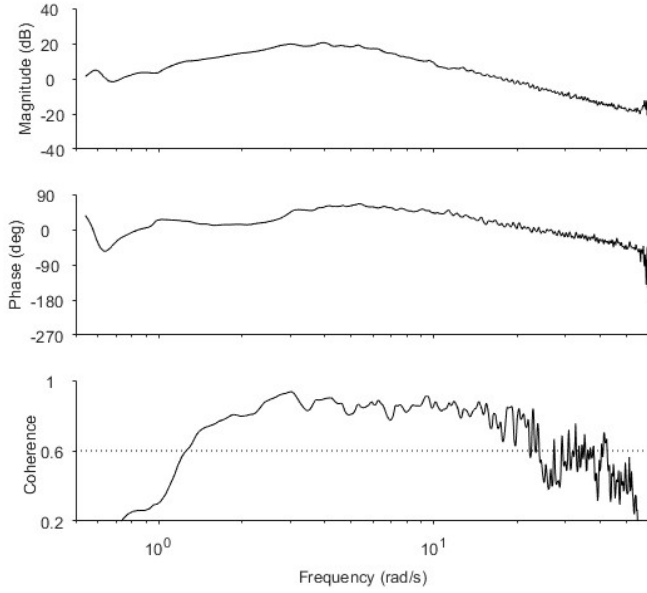**Figure 5. Frequency Response of Reference Input-Output Pair (q/δ_{thr}).**

Figure 6. Frequency Response of Input-Output Pair Obtained using JIO Method (q/δ_{col}).

Figure 7. Sample Transfer Function Identification Result (p/δ_{lat})

As shown, despite the highly correlated input present in the flight test data between δ_{col} and δ_{lon}, JIO method was able to successfully obtain an accurate frequency response for an unstable off-axis response as seen from the increased phase margin at 3dB.

Transfer Function Model Identification

In order to obtain initial estimates of the state-space model parameters, transfer function models were first identified. Primary on-axis responses for each axis was used to identify transfer function models. This was accomplished using CIFER®'s NAVFIT module (Ref. 1). The transfer function model structures are shown in Equations 5 through 8 as discussed in Ref. 4 and Ref. 5. Frequency range for the identification was limited to 1 to 15 rad/s in order to exclude the motor dynamics present at higher frequencies.

$$\frac{p}{\delta_{lat}} = \frac{L_{\delta lat}\, s\, (s-Y_v)\, e^{-\tau_{lat}s}}{s^3-Y_v s^2-L_v g} \tag{5}$$

$$\frac{q}{\delta_{lon}} = \frac{M_{\delta lon}\, s\, (s-X_u)\, e^{-\tau_{lon}s}}{s^3-X_u s^2+M_u g} \tag{6}$$

$$\frac{a_z}{\delta_{col}} = \frac{Z_{\delta col}\, s\, e^{-\tau_{col}s}}{s-z_w} \tag{7}$$

$$\frac{r}{\delta_{ped}} = \frac{N_{\delta ped}\, e^{-\tau_{ped}s}}{s-N_r} \tag{8}$$

Figure 7 shows the frequency response comparison between the identified lateral input to roll rate transfer model response and flight data.
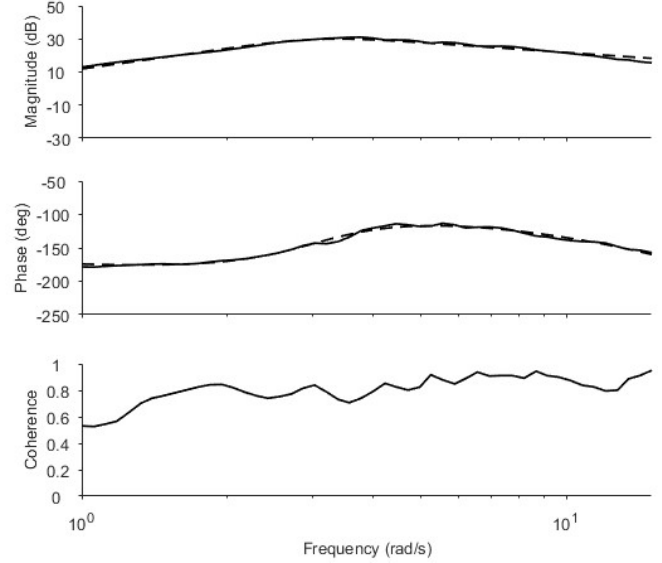
As seen in the Figure, the transfer function model response very closely follows the flight data, indicating that the identified transfer function model parameters are accurate.

The estimations of off-axis control parameters were obtained through estimating the average magnitude of the respective primary frequency response.

The identified initial model parameter estimations are shown in Table 2 and Table 3 for Y6A and Y6B, respectively.

Table 2. Y6A Initial Parameter Estimation.

Derivative	Value	Derivative	Value
$L_{\delta lat}$	118.6	$X_{\delta ped}$	-3.483
$M_{\delta lon}$	99.81	$Y_{\delta ped}$	-0.3784
$Z_{\delta col}$	-75.07	$Z_{\delta lat}$	10.00
$N_{\delta ped}$	16.05	$Z_{\delta lon}$	-3.981
Y_v	-0.02015	$Z_{\delta ped}$	-2.972
L_v	-1.246	$L_{\delta ped}$	-1.558
X_u	0.313	$M_{\delta ped}$	2.838
M_u	1.113	$N_{\delta lon}$	-0.0589
N_r	-0.7184	Z_w	-0.2937

Table 3. Y6B Initial Parameter Estimation.

Derivative	Value	Derivative	Value
$L_{\delta lat}$	123.2	N_r	-0.645
$M_{\delta lon}$	90.44	$X_{\delta col}$	5.624
$Z_{\delta col}$	-82.03	$Z_{\delta lat}$	4.315
$N_{\delta ped}$	16.28	$Z_{\delta ped}$	-4.759
Y_v	0.1566	$M_{\delta col}$	-5.395
L_v	-1.015	$N_{\delta col}$	0.1914
X_u	-0.0921	$N_{\delta lon}$	-0.9203
M_u	1.008	Z_w	-0.1989

State-Space Model Identification

The DERIVID module of CIFER® was used to identify the parameters of the state-space model. The parameters estimated using the NAVFIT module were used as the initial values of the state-space model. Certain parameters were "fixed" and held constant during the identification process.

Motor dynamics were modeled as a simple lag, with four additional states as in Ref. . The new states are denoted with lag subscript. The motor dynamics are shown in Equation 9.

$$\frac{\delta input_{lag}}{\delta input} = \frac{lag}{s+lag} \qquad (9)$$

Yaw dynamics were augmented with additional dynamics as shown below in Equation 10.

$$\frac{r_{augmented}}{\delta pe_{\;lag}}(s) = \frac{r}{\delta ped_{lag}}(s) * \frac{lead*s+1}{N_{\delta ped}} \qquad (10)$$

The state-space model structure used for the identification is given by Equation 11 (Ref. 4).

During the identification process, Cramér-Rao bounds and insensitivities were also identified. Cramér-Rao bounds were adjusted to represent 1-σ confidence intervals (Ref. 1). Parameters with excessive insensitivities or Cramér-Rao bounds were removed if the removal did not significantly affect the accuracy of the identified model.

$$
\begin{bmatrix} \dot{u} \\ \dot{v} \\ \dot{w} \\ \dot{p} \\ \dot{q} \\ \dot{r} \\ \dot{\theta} \\ \dot{\phi} \\ \dot{\psi} \\ \dot{\delta lat}_{lag} \\ \dot{\delta lon}_{lag} \\ \dot{\delta col}_{lag} \\ \dot{\delta ped}_{lag} \end{bmatrix}
=
\begin{bmatrix}
X_u & 0 & 0 & 0 & X_q & 0 & -g & 0 & 0 & 0 & X_{\delta lon} & X_{\delta col} & X_{\delta ped} \\
0 & Y_v & 0 & Y_p & 0 & 0 & 0 & g & 0 & Y_{\delta lat} & 0 & 0 & 0 \\
Z_u & Z_v & Z_w & Z_p & Z_q & Z_r & 0 & 0 & 0 & Z_{\delta lat} & Z_{\delta lon} & Z_{\delta co} & Z_{\delta ped} \\
0 & L_v & 0 & L_p & 0 & 0 & 0 & 0 & 0 & L_{\delta lat} & 0 & 0 & L_{\delta ped} \\
M_u & 0 & 0 & 0 & M_q & M_r & 0 & 0 & 0 & 0 & M_{\delta lo} & M_{\delta col} & M_{\delta ped} \\
N_u & 0 & 0 & 0 & N_q & N_r & 0 & 0 & 0 & 0 & N_{\delta lon} & N_{\delta co} & N_{\delta ped}-lag*lead \\
0 & 0 & 0 & 0 & 1 & 0 & 0 & 0 & 0 & 0 & 0 & 0 & 0 \\
0 & 0 & 0 & 1 & 0 & 0 & 0 & 0 & 0 & 0 & 0 & 0 & 0 \\
0 & 0 & 0 & 0 & 0 & 1 & 0 & 0 & 0 & 0 & 0 & 0 & 0 \\
0 & 0 & 0 & 0 & 0 & 0 & 0 & 0 & 0 & -lag & 0 & 0 & 0 \\
0 & 0 & 0 & 0 & 0 & 0 & 0 & 0 & 0 & 0 & -lag & 0 & 0 \\
0 & 0 & 0 & 0 & 0 & 0 & 0 & 0 & 0 & 0 & 0 & -lag & 0 \\
0 & 0 & 0 & 0 & 0 & 0 & 0 & 0 & 0 & 0 & 0 & 0 & -lag
\end{bmatrix}
\begin{bmatrix} u \\ v \\ w \\ p \\ q \\ r \\ \theta \\ \phi \\ \psi \\ \delta lat_{lag} \\ \delta lon_{lag} \\ \delta col_{lag} \\ \delta ped_{lag} \end{bmatrix}
$$

$$
+
\begin{bmatrix}
0 & 0 & 0 & 0 \\
0 & 0 & 0 & 0 \\
0 & 0 & 0 & 0 \\
0 & 0 & 0 & 0 \\
0 & 0 & 0 & 0 \\
0 & 0 & 0 & lag*lead \\
0 & 0 & 0 & 0 \\
0 & 0 & 0 & 0 \\
0 & 0 & 0 & 0 \\
lag & 0 & 0 & 0 \\
0 & lag & 0 & 0 \\
0 & 0 & lag & 0 \\
0 & 0 & 0 & lag
\end{bmatrix}
\begin{bmatrix} \delta lat(t-\tau_{lat}) \\ \delta lon(t-\tau_{lon}) \\ \delta col(t-\tau_{col}) \\ \delta ped(t-\tau_{ped}) \end{bmatrix} \qquad (11)
$$

The resulting model converged with the cost function of J_{avg} ≈ 59 for Y6A, and J_{avg} ≈ 55 for Y6B, which fits the guideline for a good model ($J_{avg} \leq 100$) (Ref. 1). The final identified parameters are shown in Table 4 and Table 5 for Y6A and Y6B, respectively.

Table 4. Y6A Final Identified Model Parameters.

Engineering Symbol	Value	Cramer-Rao Bounds (%)	Insensitivity (%)
$\tau_{\delta col}$	0.01597	15.39	7.418
$\tau_{\delta lat}$	0.01829	6.473	2.976
$\tau_{\delta lon}$	0.01978	6.193	2.834
$\tau_{\delta ped}$	0.02109	8.923	3.985
Lag	-13.8	3.346	0.9056
Lead	-1.822	6.9	3.199
L_{ped}	†		
$L_{\delta lat}$	130.6	2.876	0.8446
L_p	-2.116	10.33	3.944
L_v	-1.502	5.105	1.516
$M_{\delta col}$	29.27	3.666	1.298
$M_{\delta lon}$	106.2	2.623	0.794
$M_{\delta ped}$	27.14	2.445	0.834
M_q	-1.058	11.56	3.574
M_r	*		
M_u	1.107	3.529	0.9538
$N_{\delta col}$	†		
$N_{\delta lon}$	†		
$N_{\delta ped}$	14.26	5.686	2.799
N_q	†		
N_r	-0.7184‡		
N_u	†		
$X_{\delta col}$	-17.66	12.34	4.4
$X_{\delta lon}$	-15.16	2.991	0.9268
$X_{\delta ped}$	-4.534	3.834	1.467
X_q	*		
X_u	-0.3342	4.149	1.596
$Y_{\delta lat}$	17.11	3.402	1.087
Y_p	*		
Y_v	-0.3696	6.597	2.501
$Z_{\delta col}$	-79.17	4.101	1.972
$Z_{\delta lat}$	9.647	4.835	2.25
$Z_{\delta lon}$	-4.978	5.137	2.359
Z_p	*		
$Z_{\delta ped}$	-3.305	5.665	2.787
Z_q	*		
Z_r	*		
Z_u	*		
Z_v	*		
Z_w	-0.2937‡		

* Parameters removed during identification.

†Parameter removed due to negligible response pair

‡Parameter fixed during identification

Table 5. Y6B Final Identified Model Parameters.

Engineering Symbol	Value	Cramer-Rao Bounds (%)	Insensitivity (%)
$\tau_{\delta col}$	0.01342	13.38	6.043
$\tau_{\delta lat}$	0.01602	8.039	3.661
$\tau_{\delta lon}$	0.02013	6.606	2.962
$\tau_{\delta ped}$	0.02198	12.02	5.531
Lag	-13.71	3.413	0.9226
Lead	-1.797	7.947	3.574
L_{ped}	-5.541	3.835	1.887
$L_{\delta lat}$	130.1	3.047	0.921
L_p	*		
L_v	-0.9303	5.122	1.699
$M_{\delta col}$	-35.06	2.613	0.97
$M_{\delta lon}$	95.2	2.683	0.8343
$M_{\delta ped}$	†		
M_q	-0.5962	28.23	7.85
M_r	†		
M_u	0.8898	4.631	1.153
$N_{\delta col}$	-7.061	5.332	2.354
$N_{\delta lon}$	3.224	5.948	2.775
$N_{\delta ped}$	15.45	6.745	2.956
N_q	0.1925	14.27	4.3
N_r	-0.8099	15.5	6.487
N_u	-0.05146	29.53	8.99
$X_{\delta col}$	4.758	4.976	2.124
$X_{\delta lon}$	-12.79	3.32	1.092
$X_{\delta ped}$	†		
X_q	-0.2451	17.55	6.102
X_u	-0.2558	6.024	2.021
$Y_{\delta lat}$	17.03	3.718	1.287
Y_p	0.3025	17.87	7.641
Y_v	-0.2485	7.912	2.746
$Z_{\delta col}$	-80.24	4.251	2.001
$Z_{\delta lat}$	7.584	5.101	2.346
$Z_{\delta lon}$	†		
Z_p	*		
$Z_{\delta ped}$	-5.228	5.176	2.553
Z_q	†		
Z_r	*		
Z_u	†		
Z_v	*		
Z_w	-0.4164	23.66	11.43

* Parameters removed during identification.

†Parameter removed due to negligible response pair

The identified parameters for both configurations have low insensitivities and Cramér-Rao bounds, indicating that the model structures have been reduced until no extraneous parameters were left.

To assess the accuracy of the identified models, the frequency responses of the identified models were compared with the flight test data. Figure 8 and Figure 9 show the frequency response compared with flight data for vertical acceleration and pitch rate in response to longitudinal and collective input for Y6A and Y6B configurations, respectively.
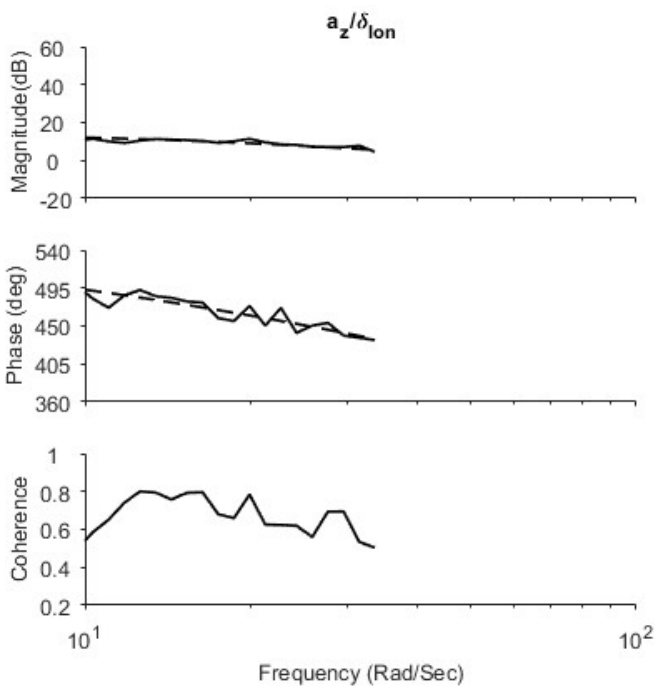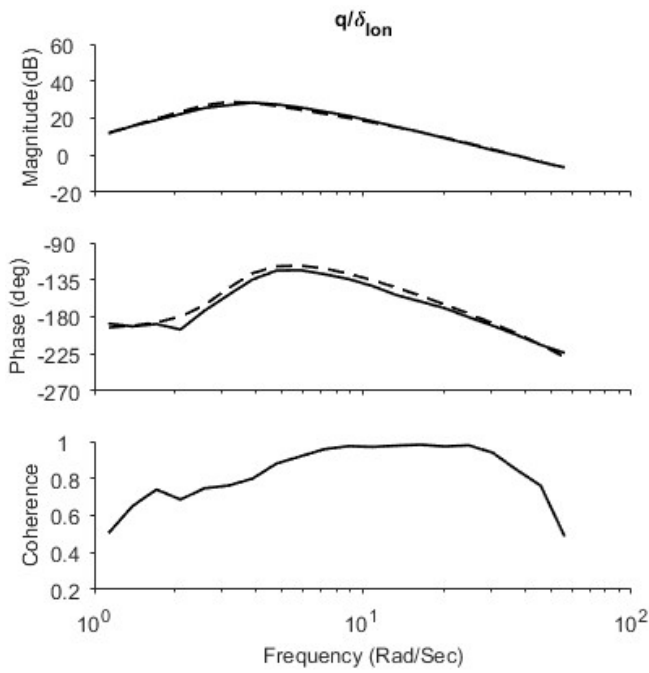
6

Figure 8. Frequency Response Comparison between Flight Data (Solid) and Model Response (Dotted) for Pitch Rate and Vertical Acceleration of Y6A Configuration.
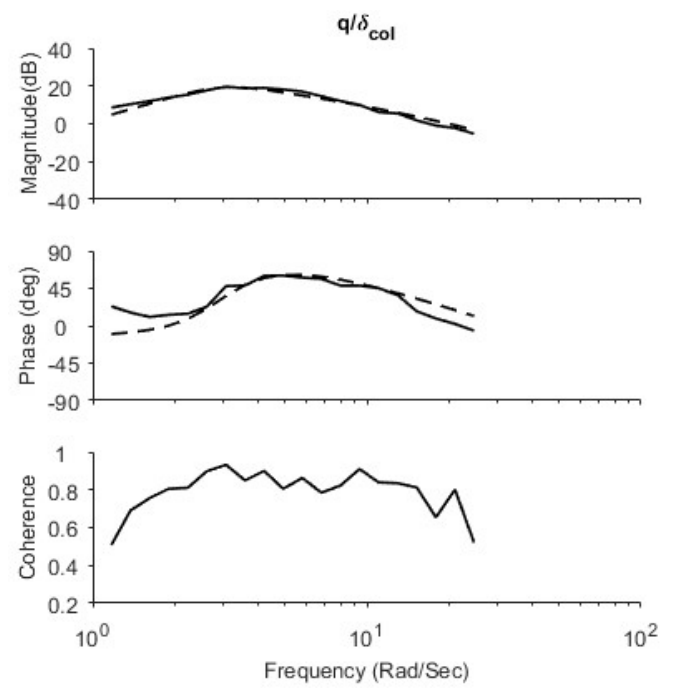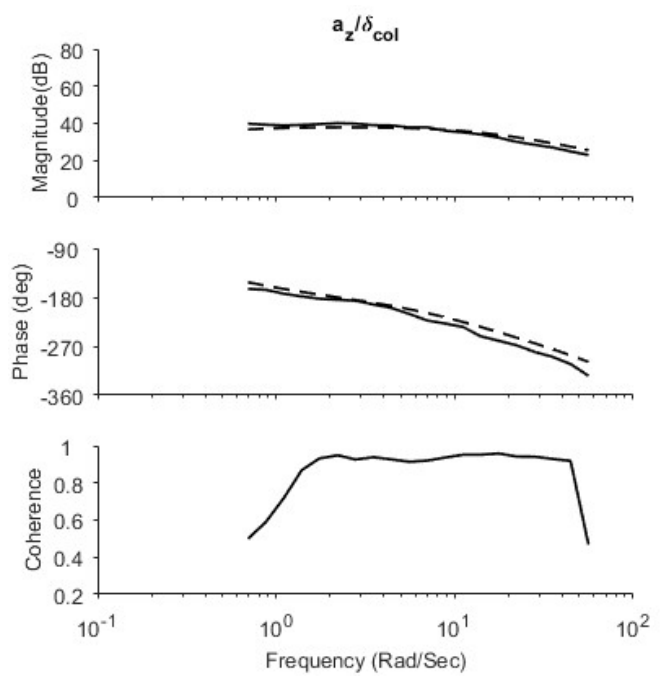
Figure 9. Frequency Response Comparison between Flight Data (Solid) and Model Response (Dotted) for Vertical Acceleration and Pitch Rate of Y6B Configuration.

It is seen from the above figures that the identified model response compare very well with the flight data, indicating that the model parameters were identified accurately.

Time-Domain Verification

In order to ensure that the identified have good predictive accuracy, time-domain verification was performed using

doublet maneuvers for each axes as it is a dissimilar maneuver from the sweeps that were used to identify the model. The VERIFY module of the CIFER® software package was used for this step (Ref. 1). The VERIFY module is capable of identifying state biases as well as output reference shifts. The verification results are shown in Figure 9 and Figure 10, for Y6A and Y6B respectively.
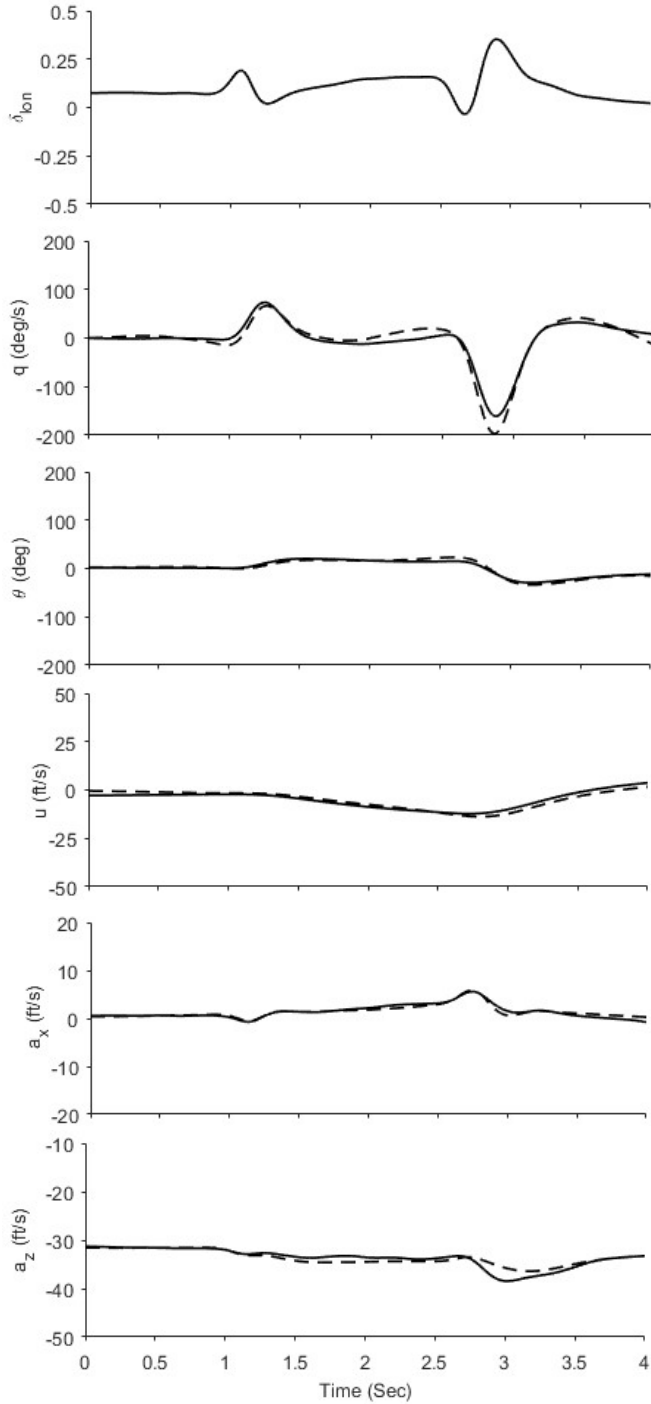

Figure 10. Time-Domain Comparison between Flight Data (Solid) and Model Responses (Dotted) for Longitudinal Input, Y6A.

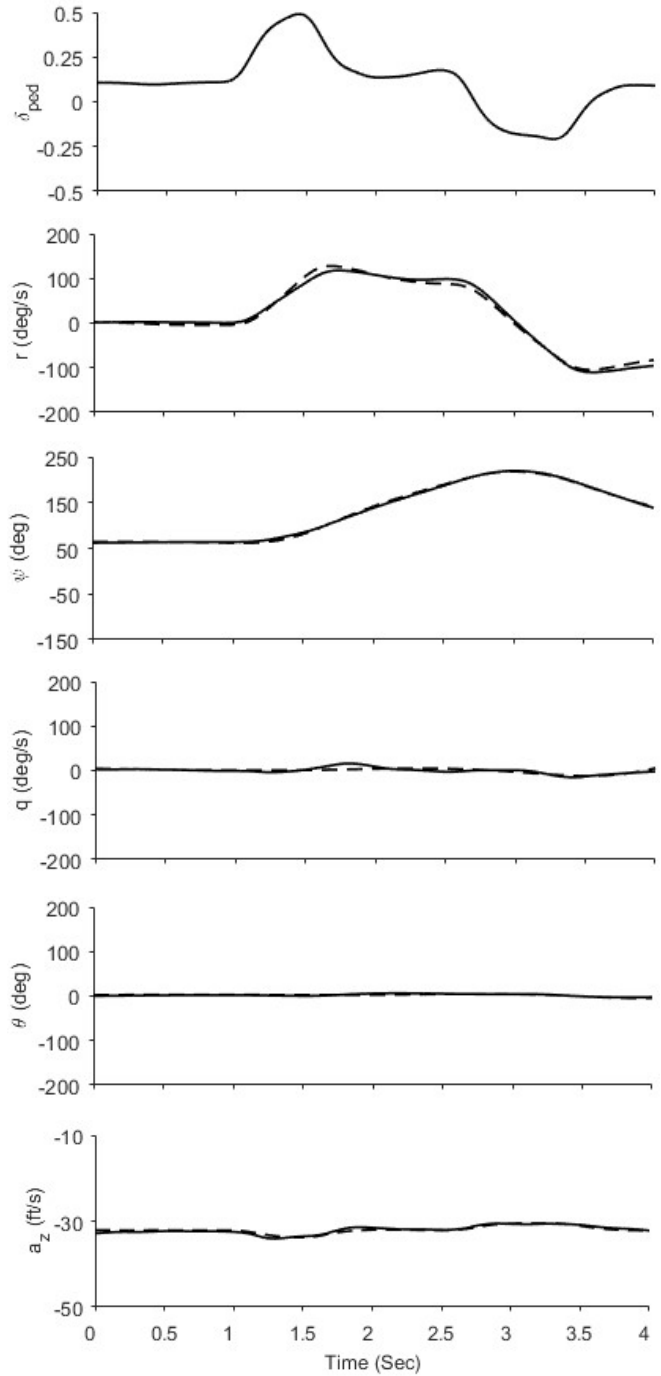**Figure 11. Time-Domain Comparison between Flight Data (Solid) and Model Responses (Dotted) for Pedal Input, Y6B.**

It can be seen that the on-axis responses are able to track the flight test data very closely, even for large amplitudes. The off-axis responses are also able to track the flight data, and accurately capture the trend of the off-axis responses even when the responses reach high amplitude.

8

OBSERVATION OF Y6 DYNAMICS

Y6 Hover/Low Speed Dynamics

The coaxial tricopter configuration of Y6 exhibits unique dynamics when compared to traditional multirotors as well as coaxial quadrotors. Traditional multirotors and coaxial quadrotor hover/low speed dynamics are completely decoupled as discussed in Ref. 4 and Ref. 5. However, both the Y6A and Y6B have different coupled dynamics, as shown by the existence of coupled derivatives such as $X_{\delta ped}$, and $Z_{\delta ped}$.

The Y6A configuration exhibits coupled dynamics in directional-longitudinal, longitudinal-heave, lateral-heave, and directional-heave, while Y6B configuration exhibits coupled dynamics in heave-longitudinal, longitudinal-directional, lateral-heave, directional-lateral, and directional-heave. It should be noted that these coupled dynamics are one-way, i.e., directional input results in heave motion, but collective input does not result in directional motion.

In an ideal setting, the moments and forces from every motor should cancel out to have completely decoupled dynamics similar to other multirotors. The coupled dynamics are most likely due to decreased rotor forces in the lower rotors, resulting from aerodynamic interference as discussed in Ref. 6. Due to the interactions between top and bottom rotors, lower rotors are not as efficient as the upper rotors, causing a force and moment imbalance that causes the coupled dynamics. The coaxial quadrotor configuration does not suffer from this issue as its propeller configuration allows for the inefficient rotors to cancel each other out.

The flight dynamic modes of both the configurations are shown in Table 6 which shows that the hover dynamic modes are highly unstable, similar to all other multirotors.

Table 6. Y6 Hover Dynamic Modes.

Modes	3DR Y6A		3DR Y6B	
	ω (rad/s)	ζ	ω (rad/s)	ζ
Lat	4.60		3.16	
	3.24	-0.33	3.08	-0.47
Lon	3.79		3.33	
	3.07	-0.39	2.93	-0.42
Col	0.29		0.42	
Ped	0.72		0.81	
Motor	13.8		13.7	

Comparison with 3DR X8+

The model parameter and dynamics of Y6 was compared with that of 3DR X8+, a coaxial quadrotor with similar physical characteristics that was previously identified in Ref. 4. The comparison of the dynamic modes of the 3DR Y6B and 3DR X8+ is shown in Table 7, which shows that the dynamic modes of both vehicles in hover are very similar.

Table 7. Y6B and X8+ Hover Dynamic Modes.

Modes	3DR Y6B		3DR X8+	
	ω (rad/s)	ζ	ω (rad/s)	ζ
Lat	3.16		3.90	
	3.08	-0.47	3.68	-0.47
Lon	3.33		4.16	
	2.93	-0.42	3.84	-0.46
Col	0.42			
Ped	0.81		0.54	
Motor	13.7		17.50	

Table 8 shows that most of the parameters are similar in value except the coupled derivatives that do not exist for the 3DR X8+, as well as increased control power of the X8+ due to increase in the number of motors.

Table 8. Comparison of Hover Model Parameters.

Parameter	3DR Y6A	3DR Y6B	3DR X8+
$\tau_{\delta col}$	0.01597	0.01342	0.0192
$\tau_{\delta lat}$	0.01829	0.01602	0.01747
$\tau_{\delta lon}$	0.01978	0.02013	0.01718
$\tau_{\delta ped}$	0.02109	0.02198	0.02915
Lag	-13.8	-13.71	-17.5
Lead	-1.822	-1.797	-3.169
L_{ped}	0	-5.541	0
$L_{\delta lat}$	130.6	130.1	157.3
L_p	-2.116	0	0
L_v	-1.502	-0.9303	-1.644
$M_{\delta col}$	29.27	-35.06	0
$M_{\delta lon}$	106.2	95.2	148.7
$M_{\delta ped}$	27.14	0	0
M_q	-1.058	-0.5962	0
M_u	1.107	0.8898	1.912
$N_{\delta col}$	0	-7.061	0
$N_{\delta lon}$	0	3.224	0
$N_{\delta ped}$	14.26	15.45	18.51
N_q	0	0.1925	0
N_r	-0.7184	-0.8099	-0.5392
N_u	0	-0.05146	0
$X_{\delta col}$	-17.66	4.758	0
$X_{\delta lon}$	-15.16	-12.79	-17.97
$X_{\delta ped}$	-4.534	0	0
X_q	0	-0.2451	0
X_u	-0.3342	-0.2558	-0.6112
$Y_{\delta lat}$	17.11	17.03	18.49
Y_p	0	0.3025	0
Y_v	-0.3696	-0.2485	-0.4277
$Z_{\delta col}$	-79.17	-80.24	-82.28
$Z_{\delta lat}$	9.647	7.584	0
$Z_{\delta lon}$	-4.978	0	0
$Z_{\delta ped}$	-3.305	-5.228	0
Z_w	-0.2937	-0.4164	0

CONCLUSIONS

1) Using frequency-domain system identification technique and joint input-output method, flight dynamics models of a

3DR Y6 tricopter were identified and verified using the flight data for two configurations (Y6A and Y6B).

2) It was found that the coaxial tricopter, in both its Y6A and Y6B configurations, exhibits unique coupled hover dynamics not found in other multirotor configurations such as coupled directional-heave motion.

3) The vehicle exhibits highly unstable modes, similar to standard multirotors and coaxial quadrotors.

4) It was seen that the model responses followed the flight data very well for both the configurations, thus providing confidence in the accuracy of the identified model.

Author contact: Sung Hyeok Cho shcho@cpp.edu
Vanessa Gonzalez vdgonzales@cpp.edu
Subodh Bhandari sbhandari@cpp.edu
Kenny Cheung: kcheung@usra.edu

REFERENCES

1. Tischler, M. B., and Remple R. K., *Aircraft and rotorcraft System Identification Second Edition*, American Institute of Aeronautics and Astronautics, Reston, VA, August 2012.

2. Berger, T., Tischler, M. B., Knapp., M. E., and Lopez, M. J. S. "Identification of Multi-Input Systems in the Presence of Highly-Correlated Inputs," *Journal of Guidance, Control, and Dynamics*, Vol. 41 (10), October 2018.

3. *Connect ESCs and Motors – Copter Documentation*, ArduPilot.org.

4. Cho, S. H., Bhandari, S., Sanders, F. C., Tischler, M. B., and Cheung, K. K., "System Identification and Controller Optimization of Coaxial Quadrotor UAV in Hover," AIAA SciTech 2019 Forum, San Diego, CA, January 2019.

5. Wei, W., Tischler, M. B., and Cohen K., "System Identification and Controller Optimization of a Quadrotor Unmanned Aerial Vehicle in Hover," *Journal of the American Helicopter Society,* Vol. 62, (4), October 2017, pp 1-9(9).

6. Prior, S. D., "Reviewing and Investigating the Use of Co-Axial Rotor Systems in Small UAVs," *International Journal of Micro Air Vehicles*, Vol. 2, (1), March 2010, pp 1-16.